

Dan Tao (Corresponding author):

Affiliation: Space Science Institute, School of Astronautics, Beihang University, Beijing, China; Dipartimento di Fisica, Università di Trento, Trento, Italy;

Address: N.37, Xueyuan Road, Haidian District, Beijing, China;

Tel: +86 010 82317921;

Email: dan.tao.unitn@outlook.com.

Roberto Battiston:

Affiliation: Dipartimento di Fisica, Università di Trento, Trento, Italy; Istituto Nazionale di Fisica Nucleare (INFN)-Trento Center for Fundamental Physics and Applications (TIPFA), Trento, Italy; Agenzia Spaziale Italiana, Roma, Italy;

Address: Via Sommarive 14, I-38123 Povo (TN), Trento, Italy;

Tel: +39 0461 281590;

Email: roberto.battiston@unitn.it.

Vincenzo Vitale:

Affiliation: Istituto Nazionale di Fisica Nucleare (INFN), sez. Tor Vergata and ASI Science Data Center, Roma, Italy;

Address: Via del Politecnico snc, 00133 Roma, Italy;

Tel: +39 0685 67868;

Email: vvitale@roma2.infn.it.

William J. Burger:

Affiliation: Istituto Nazionale di Fisica Nucleare (INFN)-Trento Center for Fundamental Physics and Applications (TIPFA), Trento, Italy; Fondazione Bruno Kessler (FBK), Trento, Italy;

Address: Via Sommarive 14, I-38123 Povo (TN), Trento, Italy;

Email: william.burger@cern.ch.

Ignazio Lazzizzera:

Affiliation: Dipartimento di Fisica, Università di Trento, Trento, Italy; Istituto Nazionale di Fisica Nucleare (INFN)-Trento Center for Fundamental Physics and Applications (TIPFA), Trento, Italy;

Address: Via Sommarive 14, I-38123 Povo (TN), Trento, Italy;

Tel: +39 0461 281551;

Email: ignazio.lazzizzera@unitn.it.

Jinbin Cao:

Affiliation: Space Science Institute, School of Astronautics, Beihang University, Beijing, China;

Address: N.37, Xueyuan Road, Haidian District, Beijing;

Tel: +86 010 82317921;

Email: jbcao@buaa.edu.cn.

Xuhui Shen:

Affiliation: Institute of Earthquake Science, China Earthquake Administration, Beijing, China;

Address: N.63, Fuxing Road, Haidian District, Beijing;

Tel: +86 010 88015464;

Email: shenxh@seis.ac.cn.

‘This work was supported by the [NASA] under Grant [number NAS5-01072]; [ASI Science Data Center (ASDC)] under Grant [number 2014-037-R.0].’

To appear in the *International Journal of Remote Sensing*
Vol. 00, No. 00, Month 20XX, 2–15

A new method to study time correlation between Van Allen Belt electrons and earthquakes

Dan Tao^{*†‡}, Roberto Battiston^{‡§¶}, Vincenzo Vitale^{||}, William J. Burger^{§††}, Ignazio Lazzizzera^{‡§}, Jinbin Cao[†], Xuhui Shen^{‡‡}

[†]*Space Science Institute, School of Astronautics, Beihang University, Beijing, China;*

[‡]*Dipartimento di Fisica, Università di Trento, Trento, Italy;* [§]*Istituto Nazionale di Fisica Nucleare (INFN)-Trento Center for Fundamental Physics and Applications (TIPFA), Trento, Italy;*

[¶]*Agenzia Spaziale Italiana, Roma, Italy;* ^{||}*Istituto Nazionale di Fisica Nucleare (INFN), sez. Tor Vergata and ASI Science Data Center, Roma, Italy;*

^{††}*Fondazione Bruno Kessler (FBK), Trento, Italy;* ^{‡‡}*Institute of Earthquake Science, China Earthquake Administration, Beijing, China.*

(Received 00 Month 20XX; accepted 00 Month 20XX)

A new method to study a possible temporal correlation between hundreds of keV Van Allen Belt electrons and strong earthquakes is proposed. It consists in measuring the electrons pitch angle distribution (PAD), searching for PAD disturbances and studying the time correlation between these PAD disturbances and strong earthquakes, occurring within a defined time window. The method was applied to measurements of energetic electrons, which were performed with the ECT-MagEIS detector on board of the Van Allen Probes mission and strong continental earthquakes, with $M \geq 5.0$ and hypocenter depth ≤ 100 km. We report the correlation studies for electrons with energies of ~ 350 keV, with which a 3.84 standard deviations correlation peak was found at $+ [0, 3]$ h time bin, and ~ 450 keV with which no correlation peaks above 2.0 standard deviations were found. Our work proves the feasibility of the proposed method and the obtained results add useful and additional information with respect to past studies.

Keywords: time correlation; satellite observations; inner radiation belt; flux; earthquake prediction.

*Corresponding author. Email: dan.tao.unitn@outlook.com

1. Introduction

In the last two decades, preseismic variations of particle fluxes beneath the lower boundary of the inner radiation belt have been reported several hours prior to earthquakes with strong magnitude. **These preseismic anomalies are still the object of investigation and debated.** Trapped electrons with energies above few MeV might precipitate as a result of mirror point lowering and pitch angle diffusion (Aleshina et al.,1992;Galper et al.,1995) after interaction with possible preseismic low-frequency (ULF/ELF) electromagnetic emissions (EME) produced in the seismic area and which are believed to propagate as Alfvén waves along geomagnetic field lines and up to the inner Van Allen radiation belt. More importantly, some interesting relevant observations exist. Particle bursts (PBs), a kind of particle fluxes characterized by an anomalous short-term and sharp increase of high-energy particle counting rates (CRs), have been observed by several satellites and correlated with strong earthquakes occurrence (Pustovetov and Malyshev 1993; Ginzburg et al. 1994; Galper, Koldashov, and Voronov 1995). A representation of a possible model explaining these results is presented in Figure 1.

In order to understand how preseismic PBs detection could be detected using space detectors, the longitudinal drift period of particles is a crucial factor which needs to be taken into account. According to Walt (1994), the drift period of electrons and protons of several tens of MeV is of the order of several tens of minutes. During this time, particles precipitated from the radiation belt may drift longitudinally around the Earth along the L -shell corresponding to the EME ground source location (Galper, Koldashov, and Voronov 1995). Aleksandrin et al. (2003) also made attempts to confirm the preseismic characteristic of these PBs, by using PBs-EQs statistical correlations, and under the hypothesis that preseismic ULF/ELF EME wave-trapped particle interaction may cause the precipitation of radiation belt electrons and protons. Experimental data on fluxes of electrons with energy from few to hundreds of MeV, obtained from four near-Earth space detectors (MIR orbital station, METEOR-3, GAMMA and SAMPEX satellites) were analyzed statistically and resulted in a 2-5 hours precursor effect. Recently, a more detailed re-analysis of the SAMPEX database also showed a 4 hours precursor effect (Sgrigna et al. 2005). ~~Previous studies show that sub-MeV electron precipitations can be caused by several sources of electromagnetic waves.~~ Searches for possible correlation between hundreds of keV electron bursts and seismic activity have been reported in recent works, such as the two statistical studies conducted by using NOAA-POES electron data (Fidani and Battiston 2008; Battiston and Vitale 2013), the second of which with a robust hint for a lithosphere-magnetosphere coupling; Sidiropoulos et al. (2011), studied electron precipitations using DEMETER electron data, where both ground transmitters and possible correlation with earthquakes are considered. Anagnostopoulos et al. (2012) also revealed that radiation-belt electron precipitation (RBEP) bursts (energies $< \sim 500$ keV) are observed in general several days before large earthquakes in the presence of broad band (~ 1 -20 kHz) VLF waves; It is interesting that the same VLF emissions were also investigated as direct seismic precursor in Němec et al. (2008), where the VLF intensity decreases shortly before (0-4 hours) powerful earthquakes. **Recent studies of already established sources of disturbances are instead reported in the following.** The effects of powerful ground based VLF transmitters (10-25 kHz) on

the 100-600 keV electrons were observed by the DEMETER satellite (Sauvaud et al. 2008; Graf et al. 2009; Sauvaud et al. 2014). In Walt et al. (2002), the scattering of electrons by ELF/VLF electromagnetic waves into the loss cone was studied by looking at coincidence of ELF/VLF wave bursts and 155 keV electron precipitations, with the Polar satellite. Whistler-induced electron precipitations are discussed in Rodger et al. (2003). These authors investigated the significance of the lightning-generated whistlers, as also other sources, dealing with whistler frequencies up to 10 kHz and electrons of few hundreds of keV, at various L shells. Further studies on lightning-induced effects are in Inan et al. (2007) and Gemelos et al. (2009).

Almost all PBs-EQs correlation analyses were carried out in the ionosphere-magnetosphere transition region while no attempt was done to study the variations of particle fluxes in the inner radiation belt. This happened partially because of the lack of stable space observation missions in the inner belt. The used observation in past studies was the sudden increases of electron fluxes, possibly associated with the lowering of the electrons mirror points. Here instead we propose to use as observable the electrons PAD disturbances ($PAD_{\text{disturbance}}$), which also might be sensitive to the possible release of EME from the ground. The PAD can be measured within the inner radiation belt and their disturbances, in respect of the unperturbed belt electron fluxes, can be searched by comparing the observed PAD (PAD_{observed}) under study and a properly built PAD template (PAD_{template}). **If a correlation signal is found, then it is important to study possible residual effects of the already known sources of perturbances. In the case of earthquakes and few hundreds of keV electrons, this means the effects of geomagnetic activity (magnetic storms) and lightnings.** The newly available data from Magnetic Electron Ion Spectrometer (MagEIS) (Blake et al. 2013) on board the Van Allen Probes (VAPs) spacecraft (Kessel, Fox, and Weiss 2013) provide an unprecedented opportunity to study the detailed electron fluxes in the inner radiation belt and test our PAD method. Then we applied the method to ~ 350 -450 keV inner belt electrons measured with MagEIS and strong continental earthquakes.

2. Van Allen Probes mission and database

The Van Allen Probes (A and B) were launched into nearly identical orbits in August 2012 (Mauk et al. 2013). The two spacecraft carry identical state-of-the-art complements of particle and field measurements into 600 by 30500 km orbits with $\sim 10^\circ$ inclination. One spacecraft follows the other one along nearly identical orbits separated by ~ 0.05 -0.15 Re in L value and by ~ 0.3 h in MLT. Both spacecraft are close to the magnetic equator, with B/B_0 ranging from ~ 1.006 to 1.004 for Probe A and from ~ 1.003 to 1.001 for Probe B, based on the (Tsyganenko 1989) field model with $K_p = 2$, where B/B_0 is the ratio of the magnetic field intensity at the spacecraft to that at the magnetic equator (Fennell et al. 2014).

The Magnetic Electron Ion Spectrometers (MagEIS) (Blake et al. 2013) is part of the Energetic Particle, Composition, and Thermal Plasma (ECT) suite (Spence et al. 2013) on the Van Allen Probes. There are four MagEIS electron spectrometers on each of the two probes: one low-energy unit (LOW: ~ 20 -240 keV), two medium-energy units (MED35 and MED75: ~ 80 -1200 keV), and a high-energy unit (HIGH: ~ 0.8 -4.8 MeV). The data from each spectrometer are

accumulated over many angular sectors during each probe rotation to obtain pitch angle distributions. The medium-energy unit MED75, which covers the energy ranges of 230-1050 keV, is relevant to this study. This magnetic spectrometer views out a side of the spacecraft at 75° to the satellite spin axis. Each MED75 unit contains nine pixels, that is nine individual sensors, from which different energy electrons are obtained.

Some known data issues exist with the public L3 data from the RBSP-ECT Data Portal. Noise in “Pixel” 0 and 1 is present, which leads to a ~ 15 minute periodic oscillation in the fluxes from these two pixels. Therefore, we exclude the data from these two “Pixels”. In addition, measurements from the MagEIS suite in this data release have not been corrected for background contamination, resulting from both external and internal sources, which influences all of the MagEIS data at various locations along the orbit. In particular, bremsstrahlung appears to be a major source of background contamination in the LOW/MED units at energies ~ 20 -400 keV, in regions where multi-MeV (~ 2 -4 MeV) electrons are intense. Nevertheless, a good rule-of-thumb is that below about 700 keV, electron data in the inner belt is relatively safe to use. Latest results showed that there is an impenetrable barrier to ultrarelativistic electrons in the Van Allen radiation belts (Baker et al. 2014) and that the inner radiation zone contains no MeV electrons by analyzing ECT-MagEIS data (Fennell et al. 2015). Given the above facts, our study therefore focuses on hundreds of keV energetic electrons (~ 350 -450 keV) in the inner radiation belt with data from “Pixel” 3 and 4 of unit MED75-A,B (see Table 1 for details) from 7 September 2012 to 29 January 2015.

3. Data analysis

In order to focus on the inner belt data, we further filter the data, which is then analyzed with dedicated analysis codes based on the ROOT analysis package classes. The inner belt zone is defined as $1.25 \leq L^* \leq 2.45$, based on the OP77Q external field (Olson and Pfizter 1977) and IGRF internal field models, where L^* is the Roederer L shell associated with the third adiabatic invariant, i.e., the magnetic flux enclosed by the particles guiding drift shell (Roederer 1970; Koller, Reeves, and Friedel 2009; Yu, Koller, and Jordanova 2012; Yu et al. 2014).

The data processing is organized as follows. Firstly, Section 3.1 discusses the criteria of earthquakes selection and corresponding exclusion of aftershocks. Section 3.2 then describes methods of building PAD_{template} , PAD_{observed} and $PAD_{\text{disturbance}}$. Thirdly, the EQ- $PAD_{\text{disturbance}}$ correlation and relative statistical significance are performed and discussed in Section 3.3. Finally, we also carry out simulation tests on the time distributions of earthquake events in Section 3.4, in order to check whether earthquakes, with the same location of the measured ones and random time occurrences, could produce a correlation signal. Table 2, summaries the selection criteria and the methods of building PADs, which is described in detail below.

3.1. Earthquake events selection

While most of the seismic EME observations reported in literature are generally associated with moderate and strong ($M \geq 4.0$ -5.0) shallow earthquakes (Pustovetov and Malyshev 1993), earthquakes with magnitude $M \geq 5.0$ and hypocentral depth

≤ 100 km are selected in this study. Furthermore, only continental earthquakes are retained, excluding those in the oceanic crust (Oike and Ogawa 1986; Galper et al. 1989; Parrot 1994), although the absorption of EME waves in the oceanic water is questionable (Ismaguilov et al. 2001).

According to Christophersen and Smith (2000), spatial analysis of the aftershock sequences leads to the definition of an aftershock area (A km²) as a function of main shock magnitude M as Equation (1):

$$\log_{10}A = M - (3.34 \pm 0.03) \quad (1)$$

The chosen strong continental earthquakes have $M \geq 5.0$ and hypocentral depth ≤ 100 km, and we reject aftershocks within a region 3° wide of the main shock during 24 hours. Finally, among 3497 seismic events 661 strong continental main shocks satisfy all the conditions, as shown in Figure 2.

3.2. *PAD_{disturbance} events selection*

When passing through the South Atlantic Anomaly (SAA), a large amount of particles will hit the detectors and would dominate or hide other particle disturbance signal. In most of the studies mentioned above, data taken from the Low Earth Orbit (LEO) satellite missions within the SAA were discarded. However, the Van Allen Probes make its observations limited in a relatively narrow band, $\pm 10^\circ$ latitude around the equator. We have checked the altitude, magnetic field and flux distribution of electrons from MagEIS data and found that electron data are not significantly influenced by the SAA, at least within $1.25 \leq L^* \leq 2.45$. Therefore, the influence of the SAA for MagEIS data is not considered.

There are several other known sources of perturbation for the low energy electrons pitch angle distribution. Among these are lightning, emissions from ground based VLF transmitters, geomagnetic storms, sun activity, etc. To reduce the effects of geomagnetic storms and sun activity, we select time period with geomagnetic index value $A_p < 20$ and sudden ionospheric disturbance index $SID = 0$ to ensure collection of data during quiet periods for analysis.

On the ground of all these considerations, PAD_{template} is defined as follows. First of all, an observed day $D_{\text{ob},i}$, where i is the date code of VAPs' data set (7 September 2012 - 29 January 2015), is selected. Then the particle flux data from two days before and after $D_{\text{ob},i}$ are binned into a two-dimensional template matrix $\{L^*, \alpha_{\text{eq}}\}$. The two dimensions are: (i) the Roederers L^* parameter, in the range between 1.25 and 2.45, with bin width is 0.1: the restricted range is chosen in order to make our analysis in the inner radiation belt; (ii) the equatorial pitch angle (α_{eq}), calculated from the local pitch angle according to the first adiabatic invariant (magnetic moment μ), ranging between 0° and 180° , and divided into 11 bins. Using flux data from each column of the template matrix (same L^* bin and all α_{eq} bins, see Figure 4(c)), we obtain the PAD_{template} at each L^* bin. The definition of PAD_{observed} , is carried out in a similar way to PAD_{template} except that the time interval is different and defined as follows: $D_{\text{ob},i}$ is divided into 8 time bins, namely, 3 hours for each PAD_{observed} time interval. This binning is chosen because the drift period of ~ 350 -450 keV electrons, with L^* parameter in range of 1.25 to 2.45, is about 0.8-2.5 hours (Figure 3). The corresponding drift

period is obtained with the knowledge of the second adiabatic invariant, provided by a numerical integration of the equation for the angular drift velocity (Walt 1994).

Figure 4 illustrates an example with electron data from Pixel 3 of MED75/MagEIS. Here, 16 December 2012 is selected as the observed day D_{ob} . The template time period covers 14-18 December except 16 December and the observational interval is chosen from 06:00 to 09:00UTC on day of 16 December. The Van Allen Probes spacecraft passed about hundreds of times through the template matrix cells (Figure 4(a)) and several tens of times through the cells within the 3-hour observational interval (Figure 4(b)). This ensures the analysis is statistically reliable. As shown in Figure 4(c) and 4(d), the large fluxes are distributed in the heart of inner belt with $L^* = \sim 1.5\text{-}2.1$ and large $\alpha_{\text{eq}} = \sim 50^\circ\text{-}130^\circ$. In Figure 4(e), we build the $\text{PAD}_{\text{template}}$ s and $\text{PAD}_{\text{observed}}$ s in five L^* bins, [1.45,1.55], [1.75,1.85], [1.95,2.05], [2.15,2.25] and [2.35,2.45] for comparison. It's worth mentioning that the equatorial pitch angle distributions with L^* below 2.0 show a flux minima at 90° (see Figure 4(e)), and as L^* increases, the minimum at 90° disappears. In fact, in the process of our statistical analysis, this feature is almost persistently present near the magnetic equator in the heart of the inner radiation belt, which coincides well with the results of Zhao et al. (2014). The equatorial loss cone at different L^* bins is also shown to indicate where the particles will strike the atmosphere and are no longer trapped in the magnetosphere. We can clearly see from Figure 4(e) that the flux level inside the loss cone is high at bin $L^* = [1.45, 1.55]$ and decreases gradually as L^* increases.

Then, we used an index, which is sensitive to the differences bin-to-bin of the two distributions, to indicate the agreement between $\text{PAD}_{\text{template}}$ and $\text{PAD}_{\text{observed}}$. This index represents an unweighted mean square weighted deviation (κ), defined as Equation (2):

$$\kappa = \frac{1}{N-1} \sum_{j=1}^N \frac{(x_j - \bar{x}_j)^2}{\sigma_{x_j}^2} \quad (2)$$

where x_j is the average flux in each α_{eq} bin of $\text{PAD}_{\text{observed}}$, \bar{x}_j is the corresponding average flux in that of $\text{PAD}_{\text{template}}$, σ_{x_j} is the associated rms error of x_j , N is the number of available α_{eq} bins in the two PADs, and $\langle N-1 \rangle$ is the number of degrees of freedom. For each available α_{eq} bin in Eq.(2), it requires that fluxes of both $\text{PAD}_{\text{template}}$ and $\text{PAD}_{\text{observed}}$ are not empty. That is, N should not be less than 9 (there are 11 α_{eq} bins in each PAD). In principle, a value of $\kappa = 1.0$ indicates that the agreement between $\text{PAD}_{\text{template}}$ and $\text{PAD}_{\text{observed}}$ is in accord with the error variance.

As the above steps applied to the whole of VAPs' data set in our study, we obtain all κ results by comparing each $\text{PAD}_{\text{observed}}$ with corresponding $\text{PAD}_{\text{template}}$. We define $\text{PAD}_{\text{disturbance}}$ events as those $\text{PAD}_{\text{observed}}$ s which assume κ values exceed 1.0 and lie within the fraction $p = 0.01$ of all κ results with the highest values, which are when the most intense flux disturbances occur. Meanwhile, the mid-point of each observational interval is recorded as the time of each $\text{PAD}_{\text{disturbance}}$ event. The selection for $\text{PAD}_{\text{disturbance}}$ events are considered for the subsequent temporal correlation analysis with strong earthquakes on land.

Figure 5 shows an example of $PAD_{\text{disturbance}}$ event. For this example we report the evaluation of the normalized index κ , as function of time and L -shell (Figure 5(a), in color code), as also the comparison of the PAD_{observed} with related PAD_{template} (Figure 5(b)). The PAD_{observed} shows a flux decrease in the loss cone region, as compared to the PAD_{template} . This flux difference caused this event to be classified as $PAD_{\text{disturbance}}$. Also other types of difference are able to provide large values of the classification index. Together with the $PAD_{\text{disturbance}}$ it is shown an earthquake, which occurred at 12:30 on 17 December 2013, with $M = 5.5$ and hypocentral depth = 71.5 km. This earthquake is one of those which a time correlation with the proposed $PAD_{\text{disturbance}}$ is searched for.

3.3. Time difference distribution

In Section 3.1 and 3.2, we described the selection of database of strong continental earthquakes and $PAD_{\text{disturbance}}$ events. Next, the time difference ($\delta T = T_{\text{EQ}} - T_{\text{PAD}}$) between the origin of earthquake and $PAD_{\text{disturbance}}$ events is computed, where T_{EQ} is the time at which the strong continental earthquakes happen and T_{PAD} is the time at which the $PAD_{\text{disturbance}}$ event is recorded. To perform a significant statistical analysis the EQ- $PAD_{\text{disturbance}}$ temporal correlation is carried out in a time window of $\delta T_{\text{max}} = \pm 1.5$ days, centered around each earthquake event.

The resulting δT distribution is shown in Figure 6. In principal, a peak with positive time δT would indicate that $PAD_{\text{disturbance}}$ events statistically precede earthquakes occurrence. **Due to the criteria of geomagnetic activity and sudden ionospheric disturbance we applied, a fraction of events are neglected.** In Figure 6(a), with data from Pixel 3 of unit MED75-A,B, a most populated peak is evident at bin $+ [0, 3]$ h and includes 87 events. Only this peak exceeds the level of 2 standard deviation units. Figure 7 shows the counts distribution, with a Poisson distribution, and a mean value $\mu = 57.8 \pm 2.83$. The excess count reaches a value of 87, and this peak value deviates 3.84 standard deviation ($\sqrt{\mu} = 7.60$) from the mean and has a probability of $1.32e^{-4}$ to be part of the main counts distribution. In contrast to the results from the data in Pixel 3, no evident correlation is obtained when considering data collected from Pixel 4, although there are several peaks at or under the level of 2 standard deviation units. As shown in Figure 6(b), the most prominent bin $+ [6, 9]$ h has a standard deviation $\sigma \approx 2.0$ and background mean is 61.4.

Figure 8 shows the geographic distribution of the strong continental earthquakes and of the corresponding electron $PAD_{\text{disturbance}}$ events which are found to have a time difference in the time bin $+ [0, 3]$ h, namely those which populate the peak in Figure 6(a). The $PAD_{\text{disturbance}}$ events detected by spacecraft VAPs are grouped in a narrow band, $\pm 10^\circ$ latitude around the equator, while the correlated earthquakes mainly occurred in three regions: the continent of Asia, Southeast Asia and west coast of South America. While the temporally correlated earthquake zones are well delimited, the corresponding satellite $PAD_{\text{disturbance}}$ events are widely distributed at all longitudes in the equatorial plane.

3.4. Test on the time distributions of earthquake events

We examined further whether earthquakes, with the same geographic location as the measured ones in Figure 8 and random time occurrences, could produce a

correlation signal. We therefore simulated 4167 earthquake samples $EQ_{T1,i}$ each with the same number of earthquakes as the measured earthquake database. For each of these $EQ_{T1,i}$ samples we repeated the above data analysis using the real $PAD_{\text{disturbance}}$ events database (Pixel 3 - Figure 6(a)) and the simulated earthquakes. The outcome of these analysis results in 4167 time-differences (Δt), from which we built a cumulative counts distribution, in which each entry is the number of EQ - $PAD_{\text{disturbance}}$ pairs, which populate a time bin of a given Δt distribution. The cumulative counts distribution has of order 10^5 entries since we create 4167 Δt distributions, each with 24 time bins.

If no correlation signal is present the resulting EQ - $PAD_{\text{disturbance}}$ distribution is a Poisson distribution. Then our cumulative distribution would be the sum of 4167 Poisson distributions with mean values within a narrow range. If instead correlation signals would be frequent enough then deviations, such as tails, would be found in the cumulative distribution. The cumulative distribution obtained is shown in Figure 9. As a first approximation it is fitted with a single Poisson distribution function and no large deviation from the expected Poisson distribution is found, although the fit provides a χ^2/ndf of 395.1/57, where ndf is the number of degrees of freedom.

4. Conclusion and discussion

In this study we proposed a new method to investigate the possible time correlation between magnetosphere phenomena and strong continental earthquakes. In fact to our knowledge, it is the first time that this investigation is accomplished with the study of the disturbances of sub-MeV electrons PAD in the inner radiation belt.

Furthermore we applied the method to measurements of energetic electrons, which were performed with the ECT-MagEIS on Van Allen Probes mission and strong continental earthquakes. As described above, we applied selection conditions to electron data on Pixel 3 and Pixel 4 of MED75/MagEIS and to the considered earthquake samples. Then we considered the time difference between the occurrence of electrons $PAD_{\text{disturbance}}$ events and that of strong continental earthquakes, within a time window of ± 1.5 days. We found the number of EQ - $PAD_{\text{disturbance}}$ pairs to distribute in agreement with a Poisson distribution. For Pixel 3 we found the most populated bin of the time difference distribution to be at $+ [0, 3] \text{h}$, with a significance of 3.84σ . For Pixel 4 most populated bins are not the same and they do not reach a significance of 2σ . Although the peak of Pixel 3 might be considered a hint that hundreds of keV electron $PAD_{\text{disturbance}}$ occur some hours before major earthquakes, similarly to results obtained with past satellite missions, the significance for the fluctuation of Pixel 3 is low and it is not supported by the identical analysis on the adjacent energy bin. It should be noted that for non-background free measurements as the current one, a statistical significance threshold of 5σ is usually required for establishing unambiguously a signal.

Furthermore to minimize possible spurious effects, also due to unknown time-structured backgrounds, if existing, it might be useful to couple the search for time correlation with other requirements, such as simultaneous time-space correlation (Ambrogini et al. 2014).

The application of our method to the MagEIS data provides useful and additional information with respect to the rare previous studies of similar quality. **However, it should be noted that we focus on the PAD perturbation and do not investigate whether for each PAD anomaly there is a precipitation.** Anomalous electron bursts caused possibly by low-frequency EME have been observed several hours prior to earthquakes of moderate or strong magnitude during the past two decades, and mainly for electron energies of few MeV and below the low boundary of the inner radiation belt. This preseismic character of anomalous bursts of electron fluxes is still an open question and debated. Our results provide also a contribution to this debate and give useful information for its possible further optimization. In the next future, new measurements of energetic particles (electrons from 3-100 MeV, protons from 30-200 MeV) will be carried out with the High Energy Particle Detector (HEPD) (Battiston and Conti 2011) on board of the Chinese Electromagnetic Satellite (CSES) (Shen et al. 2011), as also simultaneous measurements of the electrical and magnetic fields and plasma in ionosphere. This satellite mission is under development will contribute valuable data for the study of earthquake precursors.

Acknowledgements

We acknowledge use of data from NASA's Van Allen Probes mission, specifically the publicly available data from the RBSPECT (Energetic Particle, Composition, and Thermal Plasma) instruments what was supported by funding under NASA's Prime contract no. NAS5-01072. We also thank the National Earthquake Information Center (NEIC) ComCat database of the U.S. Geological Survey for providing available earthquakes data and the American Association of Variable Stars Observers (AAVSO) for providing the SID data. V. Vitale acknowledges the support of the ASI Science Data Center (ASDC), Prot. Agg. Convenzione Quadro ASI-INFN N. 2014-037-R.0. This work is mainly sponsored by China Scholarship Council (CSC).

References

- Aleksandrin, S. Yu., Galper, A. M., Grishantzeva, L. A., Koldashov, S. V., Maslennikov, L. V., Murashov, A. M., Picozza, P., Sgrigna, V., and Voronov, S. A. 2003. "High-energy charged particle bursts in the near-Earth space as earthquake precursors." *Annales Geophysicae* 21: 597-602.
- Aleshina, M. E., Voronov, S. A., Galper, A. M., Koldashov, S. V., and Maslennikov, L. V. 1992. "Correlation between earthquake epicenters and regions of high-energy particle precipitations from the radiation belt." *Cosmic Research* 30(1): 79-83.
- Ambroglini F., W.J. Burger, R. Battiston, V. Vitale, and Y. Zhang. 2014. "Space Earthquake Perturbation Simulation (SEPS) an application based on Geant4 tools to model and simulate the interaction between the Earthquake and the particle trapped on the Van Allen belt." *Geophysical Research Abstracts*, Vol. 16, EGU2014-15024.
- Anagnostopoulos, G.C., Vassiliadis, E., Pulnests, S. 2012. "Characteristics of flux-time profiles, temporal evolution, and spatial distribution of radiation-belt electron precipitation bursts in the upper ionosphere before great and giant earthquakes." *Ann. of Geophysics*, 55: 21-36, doi:10.4401/ag-5365.
- Baker, D. N., A. N. Jaynes, V. C. Hoxie, R. M. Thorne, J. C. Foster, X. Li, J. F. Fennell, et al. 2014. "An impenetrable barrier to ultra-relativistic electrons in the Van Allen radiation belt." *Nature* 515: 531-534, doi:10.1038/nature13956.

- Blake, J. B., P. A. Carranza, S. G. Claudepierre, J. H. Clemmons, W. R. Crain Jr., Y. Dotan, et al. 2013. "The magnetic electron ion spectrometer (MagEIS) instruments aboard the radiation belt storm probes (RBSP) spacecraft." *Space Sci. Rev.* 179(1-4): 383-421, doi:10.1007/s11214-013-9991-8.
- Battiston, R., and Conti L. 2011. *Italian participation to the CSES project APSCO 3rd Int. Symposium*, Beijing, China, 13-15 September.
- Battiston, R. and Vitale, V. 2013. "First evidence for correlations between electron fluxes measured by NOAA-POES satellites and large seismic events." *Nuclear Physics B (Proc Suppl)* 243-244: pp. 249-257.
- Christophersen, A. and Smith, E. G. C. 2000. "A global model for aftershock behaviour." Proceedings, *12th World Conf. Earthq. Engg.*, Auckland, 2000. Paper 0379, 8pp.
- Fennell, J. F., J. L. Roeder, W. S. Kurth, M. G. Henderson, B. A. Larsen, G. Hospodarsky, J. R. Wygant, et al. 2014. "Van Allen Probes observations of direct wave-particle interactions." *Geophys. Res. Lett.* 41: 1869-1875, doi:10.1002/2013GL059165.
- Fennell, J. F., S. G. Claudepierre, J. B. Blake, T. P. O'Brien, J. H. Clemmons, D. N. Baker, H. E. Spence, and G. D. Reeves. 2015. "Van Allen Probes show that the inner radiation zone contains no MeV electrons: ECT/MagEIS data." *Geophys. Res. Lett.* 42, doi:10.1002/2014GL062874.
- Fidani, C. and Battiston, R. 2008. "Analysis of NOAA particle data and correlations to seismic activity." *Nat. Hazards Earth Syst. Sci.* 8, 1277-1291, doi:10.5194/nhess-8-1277-2008.
- Galper, A. M., Dimitrenko, V. B., Nikitina, N. V., Grachev, V. M., and Ulin, S. E. 1989. "Interrelation between high-energy charged particle fluxes in the radiation belt and seismicity of the Earth." *Cosmic Research* 27: 789.
- Galper, A. M., Koldashov, S. V., and Voronov, S. A. 1995. "High energy particle flux variations as earthquake predictors." *Advances in Space Research* 15: 131-134.
- Gemelos, E. S., U. S. Inan, M. Walt, M. Parrot, and J. A. Sauvaud. 2009. "Seasonal dependence of energetic electron precipitation: Evidence for a global role of lightning." *Geophys. Res. Lett.* 36, L21107, doi:10.1029/2009GL040396.
- Ginzburg, E. A., Malishev, A. B., Proshkina, I. P., and Pustovetov, V. P. 1994. "Correlation of strong earthquakes with radiation belt particle flux variations." *Geomagnetism and Aeronomy* 34: 315-320 (English Translation).
- Graf, K. L., U. S. Inan, D. Pidtyachiy, P. Kulkarni, M. Parrot, and J. A. Sauvaud. 2009. "DEMETER observations of transmitter-induced precipitation of inner radiation belt electrons." *J. Geophys. Res.* 114, A07205, doi:10.1029/2008JA013949.
- Inan, U. S., D. Pidtyachiy, W. B. Peter, J. A. Sauvaud, and M. Parrot. 2007. "DEMETER satellite observations of lightning-induced electron precipitation." *Geophys. Res. Lett.* 34, L07103, doi:10.1029/2006GL029238.
- Ismaguilov, V. S., Kopytenko, Yu. A., Hattori, K., Voronov, P. M., Molchanov, O. A., and Hayakawa, M. 2001. "ULF magnetic emissions connected with under sea bottom earthquakes." *Natural Hazards and Earth System Sciences* 1: 23-31.
- Kessel, R. L., N. J. Fox, and M. Weiss. 2013. "The Radiation Belt Storm Probes (RBSP) and space weather." *Space Sci. Rev.* 179(1-4): 531-543, doi:10.1007/s11214-012-9953-6.
- Koller, J., Reeves, G. D., and Friedel, R. H. W. 2009. "LANL* V1.0: a radiation belt drift shell model suitable for real-time and reanalysis applications." *Geosci. Model Dev.* 2: 113-122, doi:10.5194/gmd-2-113-2009.
- Mauk, B. H., N. J. Fox, S. G. Kanekal, R. L. Kessel, D. G. Sibeck, and A. Ukhorskiy. 2013. "Science objectives and rationale for the Radiation Belt Storm Probes mission." *Space Sci. Rev.* 179: 3-27, doi:10.1007/s11214-012-9908-y.
- Némec, F., O. Santolík, M. Parrot, and J. J. Berthelier. 2008. "Spacecraft observations of electromagnetic perturbations connected with seismic activity." *Geophys. Res. Lett.* 35, L05109, doi:10.1029/2007GL032517.
- Oike, K. and Ogawa, T. 1986. "Electromagnetic radiations from shallow earthquake observed in the LF range." *Journal of Geomagnetism and Geoelectricity* 38: 1031-1040.
- Olson, W. P., and K. A. Pfitzer. 1977. "Magnetospheric magnetic field modeling." *Annual scientific report, Air Force Off. of Sci. Res.* Contract F44620-75-C-0033, 96 pp.,

- McDonnell Douglas Astronautics Co., Huntington Beach, Calif.
- Parrot, M. 1994. "Statistical study of ELF/VLF emissions recorded by a low-altitude satellite during seismic events." *Journal of Geophysical Research* 99: 23339-23347.
- Pustovetov, V. P. and Malyshev, A. B. 1993. "Space-time correlation of earthquakes and high-energy particle flux variations in the inner radiation belt." *Cosmic Research* 31: 84-90.
- Rodger, C. J., M. A. Clilverd, and R. J. McCormick. 2003. "Significance of lightning-generated whistlers to inner radiation belt electron lifetimes." *J. Geophys. Res.* 108, 1462, doi:10.1029/2003JA009906, A12.
- Roederer, J. G. 1970. *Dynamics of Geomagnetically Trapped Radiation*. Springer, New York.
- Sauvaud, J.-A., R. Maggiolo, C. Jacquy, M. Parrot, J.-J. Berthelier, R. J. Gamble, and C. J. Rodger. 2008. "Radiation belt electron precipitation due to VLF transmitters: Satellite observations." *Geophys. Res. Lett.* 35, L09101, doi:10.1029/2008GL033194.
- Sauvaud, J.-A., Parrot, M., and Slominska, E. 2014. "Comment on "Comparative study on earthquake and ground based transmitter induced radiation belt electron precipitation at middle latitude", by Sideropoulos et al. (2011)." *Nat. Hazards Earth Syst. Sci.* 14, 1-9, doi:10.5194/nhess-14-1-2014.
- Sgrigna, V., L. Carota, L. Conti, A. M. Corsi, A. M. Galper, S. V. Koldashov, A. M. Murashov, P. Picozza, R. Scrimaglio, and L. Stagni. 2005. "Correlations between earthquakes and anomalous particle bursts from SAMPEX/PET satellite observations." *J. Atmos. Sol.-Terr. Phys* 67: 1448-1462, doi:10.1016/j.jastp.2005.07.008.
- Shen X., X. Zhang, L. Wang, H. Chen, Y. Wu, S. Yuan, J. Shen, S. Zhao, J. Qian, and J. Ding. 2011. "The earthquake-related disturbances in ionosphere and project of the first China seismo-electromagnetic satellite." *Earthq. Sci.* 24, pp. 639-650.
- Sideropoulos, N. F., Anagnostopoulos, G., and Rigas, V. 2011. "Comparative study on earthquake and ground based transmitter induced radiation belt electron precipitation at middle latitudes." *Nat. Hazards Earth Syst. Sci.* 11, 1901-1913, doi:10.5194/nhess-11-1901-2011.
- Spence, H. E., G. D. Reeves, D. N. Baker, J. B. Blake, M. Bolton, S. Bourdarie, A. A. Chan, et al. 2013. "Science goals and overview of the energetic particle, composition, and thermal plasma (ECT) suite on NASA's radiation belt storm probes (RBSP) mission." *Space Sci. Rev.* 179(1-4): 311-336, doi:10.1007/s11214-013-0007-5.
- Tsyganenko, N. A. 1989. "A magnetospheric magnetic field model with a warped tail current sheet." *Planet. Space Sci.* 37: 5-20, doi:10.1016/0032-0633(89)90066-4.
- Walt, M. 1994. *Introduction to Geomagnetically Trapped Radiation*. Cambridge University Press, Cambridge.
- Walt, M., H. D. Voss, and J. Pickett. 2002. "Electron precipitation coincident with ELF/VLF wave bursts." *J. Geophys. Res.* 107(A8), doi:10.1029/2001JA009100.
- Yu, Y., J. Koller, S. Zaharia, and V. Jordanova. 2012. "L* neural networks from different magnetic field models and their applicability." *Space Weather* 10, S02014, doi:10.1029/2011SW000743.
- Yu, Y., J. Koller, V. K. Jordanova, S. G. Zaharia, R. W. Friedel, S. K. Morley, Y. Chen, D. Baker, G. D. Reeves, and H. E. Spence. 2014. "Application and testing of the L* neural network with the self-consistent magnetic field model of RAM-SCB." *J. Geophys. Res. Space Physics* 119: 1683-1692, doi:10.1002/2013JA019350.
- Zhao, H., X. Li, J. B. Blake, J. F. Fennell, S. G. Claudepierre, D. N. Baker, A. N. Jaynes, D. M. Malaspina, and S. G. Kanekal. 2014. "Peculiar pitch angle distribution of relativistic electrons in the inner radiation belt and slot region." *Geophys. Res. Lett.* 41: 2250-2257, doi:10.1002/2014GL059725.

Table 1. Unit MED75-A,B channel Level-3 data available for this study.

(Pixel-MagEIS)	Pixel 3 (Probe A/B)	Pixel 4 (Probe A/B)
Centroid (keV)	349/353	456/459
Width (keV)	27/27	64/57
Low Bound (keV)	335/340	424/430
High Bound (keV)	363/367	488/487

Table 2. Cuts applied to data for selecting earthquakes interested and methods for building PAD_{template} and PAD_{observed} .

Earthquake Events Selection	PAD Building
Magnitude ≥ 5.0 ; Hypocentral depth ≤ 100 km; No earthquakes in the oceanic crust; Criteria for filtering aftershocks: $\delta\text{time} \leq 24\text{h}$; $\delta\text{latitude} \leq 3^\circ$; $\delta\text{longitude} \leq 3^\circ$.	SAA influence is not considered; Geomagnetic index: $A_p < 20$; Ionospheric disturbance index: $SID = 0$; Build matrix $\{L^*, \alpha_{\text{eq}}\}$: $1.25 \leq L^* \leq 2.45$ (step = 0.1); $0^\circ \leq \alpha_{\text{eq}} \leq 180^\circ$ (11 bins).
PAD_{template} Building Selected the observed day $D_{\text{ob},i}$; Define 2 days before and after $D_{\text{ob},i}$ as the template days; Fill data of template days from MagEIS A+B to build template matrix $\{L^*, \alpha_{\text{eq}}\}$.	
PAD_{observed} Building Divide $D_{\text{ob},i}$ into 8 time bins, namely, each 3 hours as an observed interval; Fill each 3 hours data from MagEIS A+B to build observed matrix $\{L^*, \alpha_{\text{eq}}\}$.	
PAD_{disturbance} Acceptance Rate Pixel 3 : 0.989e^{-2} (814/82272); Pixel 4 : 1.017e^{-2} (837/82272).	

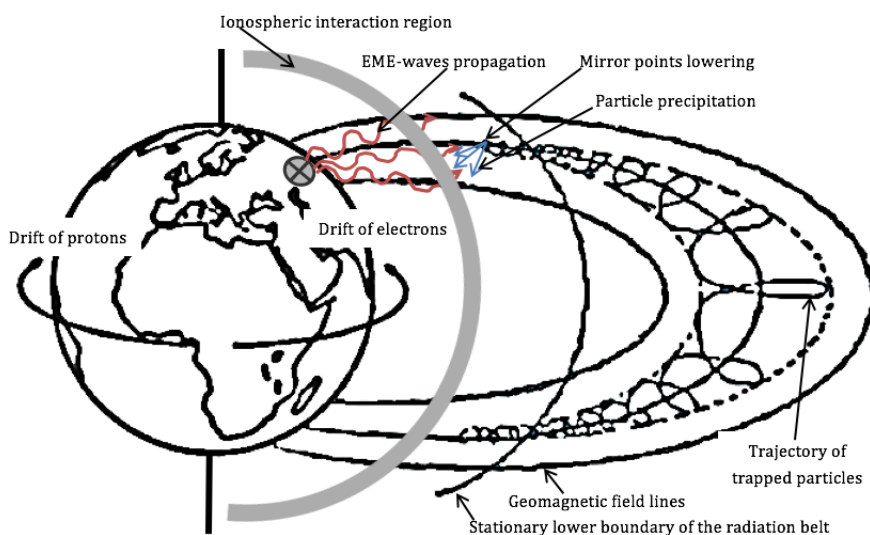


Figure 1. Schematic representation of pre-seismic electromagnetic disturbances may interact with trapped particles causing particle precipitation as a result of mirror point lowering [Adopted from Fig. 1 in Sgrigna et al. (2005)]. Pre-seismic EME waves produced in the earthquake preparation area propagate as Alfvén waves along the geomagnetic field lines. Near the boundary of radiation belt, the waves may resonantly interact with trapped particles causing particle precipitation as a result of pitch angle diffusion. Then the precipitating particle bursts drift longitudinally and are detected by spacecraft in the ionosphere-magnetosphere transition zone.

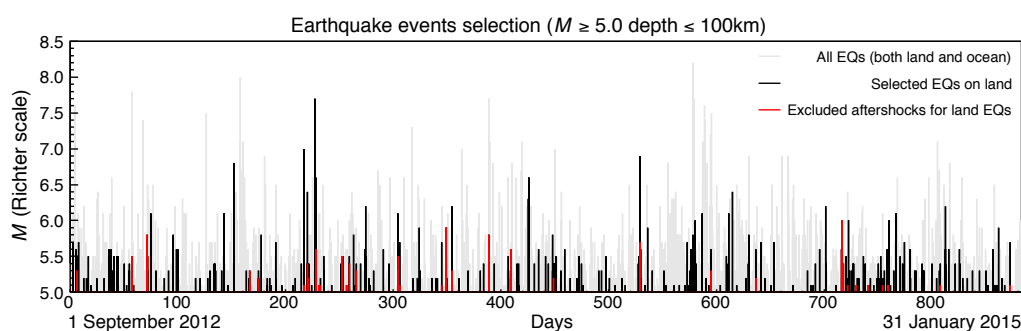


Figure 2. Global seismic activities over the period of 1 September 2012 to 31 December 2015. All earthquakes are required to have $M \geq 5.0$ and hypocentral depth ≤ 100 km. 661 continental main shocks (black) are selected from 3497 global land and oceanic seismic events (grey), and then 99 aftershocks (red) are excluded from the 661 strong ones.

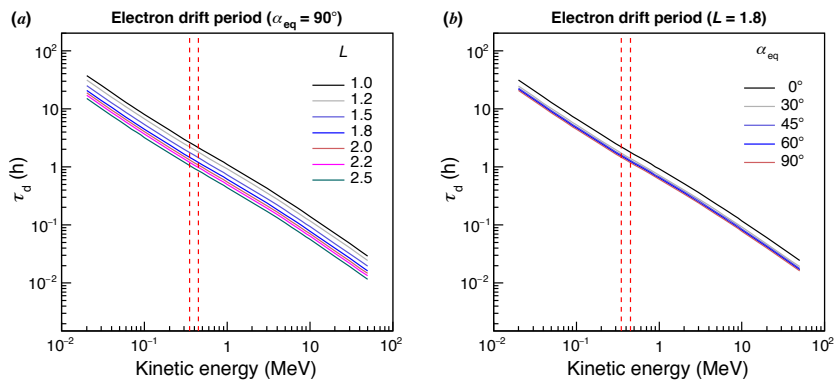


Figure 3. The drift period (τ_d) as a function of kinetic energy for different α_{eq} and L -shell values. (a) The drift period at $\alpha_{eq} = 90^\circ$ for seven different L -shell values (1.0-2.5); (b) The drift period at $L = 1.8$ for five different α_{eq} values (0° - 90°). The vertical red lines indicate the kinetic energies of 350 and 450 keV, respectively.

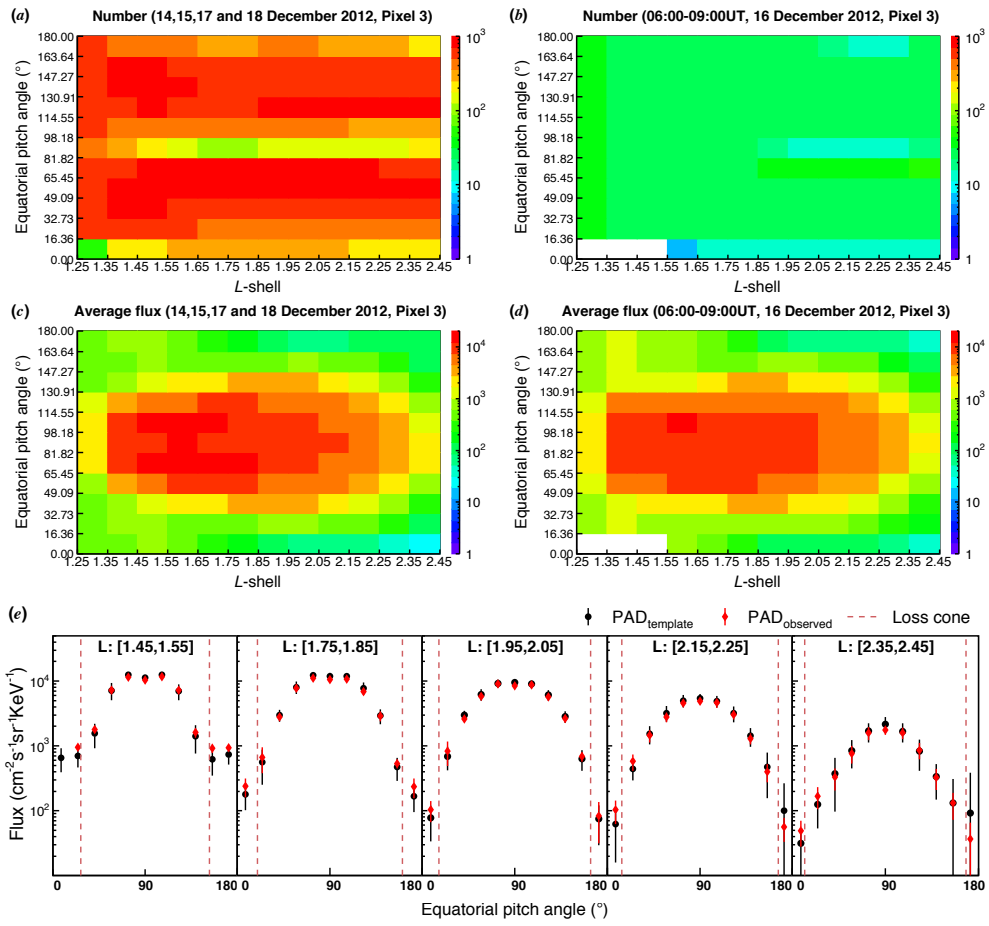


Figure 4. An example for building the PAD_{template} and PAD_{observed}. Panel (a) and (c) illustrate the number of two probes crossing and corresponding average flux values in two-dimensional $\{L^*, \alpha_{eq}\}$ template matrix; and panel (b) and (d) show that in two-dimensional $\{L^*, \alpha_{eq}\}$ observed matrix. Here, the observed day D_{ob} is 16 December 2012; The template time period covers 14-18 December except D_{ob} and the observational interval is chosen from 06:00 to 09:00UTC on day of D_{ob} . Panel (e) illustrates the PAD_{template}s and PAD_{observed}s built in five L^* bins, [1.45,1.55], [1.75,1.85], [1.95,2.05], [2.15,2.25] and [2.35,2.45], respectively. Meanwhile, the approximate width of loss cone (the red dash lines) was drawn in each sub-panel.

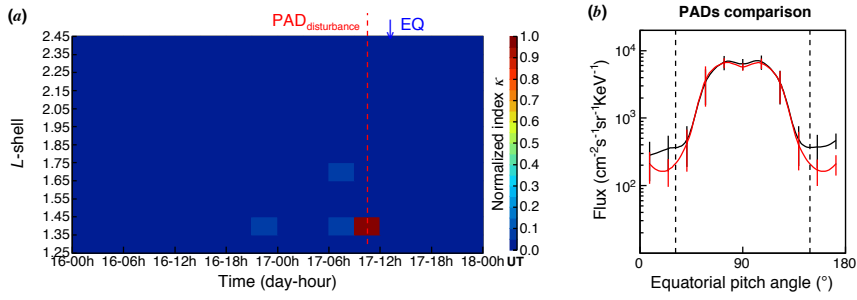


Figure 5. An example of $\text{PAD}_{\text{disturbance}}$ event. (a) Distribution of the normalized index κ versus time (16-17 December 2013) and L -shell. The red dash line illustrates the mid-point of the observational interval for the considered PAD $\{t : 09:00-12:00; L : 1.35-1.45\}$. The blue arrow labels the occurrence of a major earthquake ($25.51^{\circ}\text{S}, 70.5^{\circ}\text{W}, M-5.5$). (b) Comparison of the $\text{PAD}_{\text{observed}}$ and related $\text{PAD}_{\text{template}}$, corresponding to the $\text{PAD}_{\text{disturbance}}$ bin, which in (a) has color-code crimson. The black solid line is the $\text{PAD}_{\text{template}}$ while the red one shows the $\text{PAD}_{\text{observed}}$. Besides, two black vertical dash lines are the approximate width of loss cone.

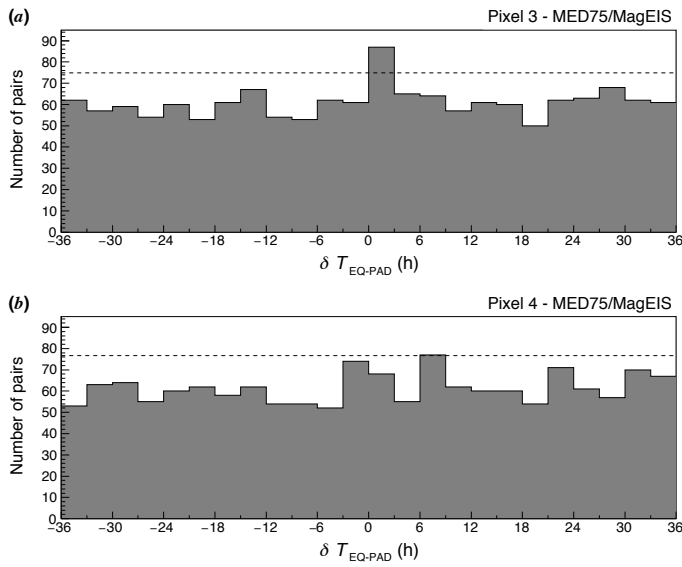


Figure 6. The time difference distribution. Here the time delays between $\text{PAD}_{\text{disturbance}}$ and strong continental earthquakes in Pixel 3 (a) and 4 (b), respectively, are plotted. EQ-PAD $_{\text{disturbance}}$ pairs are taken within a time window of ± 1.5 days. The horizontal dash lines indicate the background mean $+2\sigma$ value of each distribution.

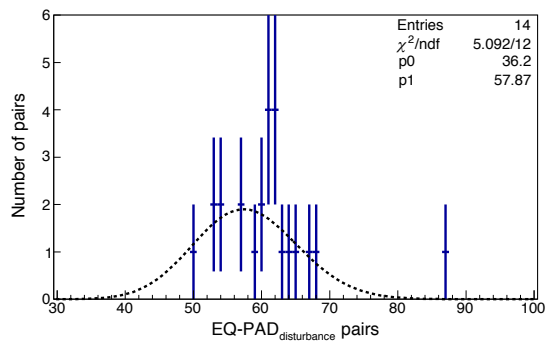


Figure 7. The EQ-PAD_{disturbance} pairs distribution. Here the number of EQ-PAD_{disturbance} pairs in each time bin in Figure 6(a) are plotted. The number of pairs distribute in agreement with a Poisson distribution, with a mean value $\mu = 57.8 \pm 2.83$. The excess counts value is at 87. This value deviates 3.84 standard deviation ($\sqrt{\mu} = 7.60$) from the distribution mean and has a probability of $1.32e^{-4}$ to be part of the main distribution.

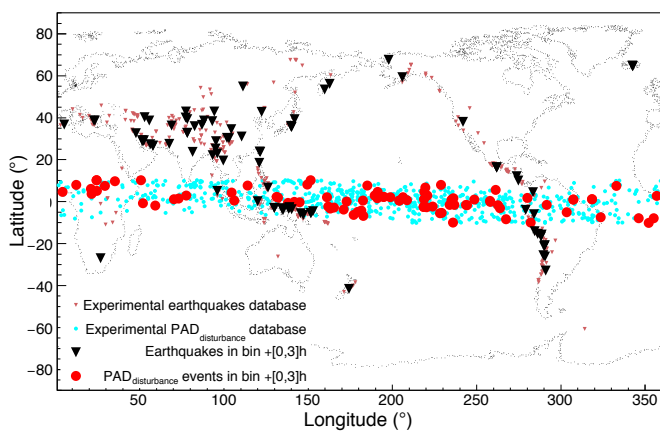


Figure 8. The geographic distribution of correlating strong continental earthquakes and electron PAD_{disturbance} events. Here are shown as color code the distribution of PAD_{disturbance} events (selected from pixel 3, as red dots) and earthquakes ($M \geq 5$, Depth ≤ 100 km, on the land, as black inverted triangles) which correlated in the populated time bin $+ [0, 3]h$.

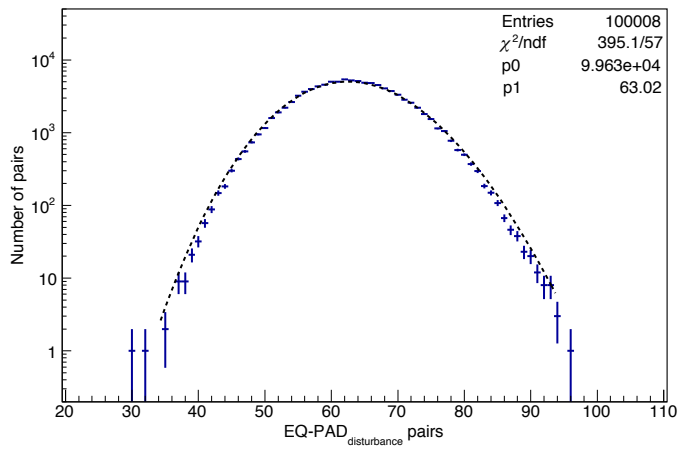


Figure 9. The counts cumulative distribution, obtained during the 4167 iterations of test. It consists of a sum of Poisson distributions, each of which having a mean slightly different from the others. A first approximation single Poisson distribution fit provides a χ^2/ndf of 395.1/57, and the distribution reaches a maximum of 96 counts (4.15σ) in 100008 trials.